*Article*

# Investigating the Effect of Heterogeneous Hull Roughness on Ship Resistance Using CFD

**Soonseok Song** [1], **Yigit Kemal Demirel** [1,*], **Claire De Marco Muscat-Fenech** [2], **Tonio Sant** [2], **Diego Villa** [3], **Tahsin Tezdogan** [1] and **Atilla Incecik** [4]

1   Department of Naval Architecture, Ocean and Marine Engineering, University of Strathclyde, Glasgow G1 0LZ, UK; soonseok.song@strath.ac.uk (S.S.); tahsin.tezdogan@strath.ac.uk (T.T.)
2   Department of Mechanical Engineering, University of Malta, Msida, MSD 2080, Malta; claire.demarco@um.edu.mt (C.D.M.M.-F.); tonio.sant@um.edu.mt (T.S.)
3   Department of Electrical, Electronic, Telecommunication Engineering and Naval Architecture, University of Genoa, Via all'Opera Pia, 11A, 16145 Genova, Italy; diego.villa@unige.it
4   Faculty of Engineering, University of Strathclyde, Glasgow G1 1XJ, UK; atilla.incecik@strath.ac.uk
*   Correspondence: yigit.demirel@strath.ac.uk; Tel.: +44-(0)1415483463

**Abstract:** Research into the effects of hull roughness on ship resistance and propulsion is well established, however, the effect of heterogeneous hull roughness is not yet fully understood. In this study, Computational Fluid Dynamics (CFD) simulations were conducted to investigate the effect of heterogeneous hull roughness on ship resistance. The Wigley hull was modelled with various hull conditions, including homogeneous and heterogeneous hull conditions. The results were compared against existing experimental data and showed a good agreement, suggesting that the CFD approach is valid for predicting the effect of heterogeneous hull roughness on ship resistance. Furthermore, the local distributions of the wall shear stress and roughness Reynolds number on the hull surface were examined to assess the flow characteristics over the heterogeneous hull roughness.

**Keywords:** roughness effect; Wigley hull; ship resistance; heterogeneous hull roughness; computational fluid dynamics (CFD)

## 1. Introduction

One of the major barriers to energy-efficient shipping is hull roughness, which is caused by various factors including mechanical causes, chemical and electrochemical processes (i.e., corrosion), and the colonisation of biofouling [1,2]. The associated economic and environmental problems include the added ship resistance and increased fuel consumption and $CO_2$ emissions, as well as the cost for the hull maintenance. From a naval architect or a ship owner's point of view, a proper life cycle assessment is needed to improve the profitability of the ship. In other words, the economic penalties associated with the increased fuel consumption and/or the speed loss of ships should be accurately predicted and compared with the costs associated with the antifouling activities.

Accordingly, there have been investigations and studies to predict the impact of hull roughness on ship performance. The similarity law scaling procedure proposed by Granville [3,4] has been preferred by many researchers, e.g., [5–9], owing to its merits including the computational cost-effectiveness and the robustness for arbitrary ship lengths and speeds [10]. However, Granville's method is still limited by the flat plate simplification, which disregards the 3D effects, e.g., form resistance [11].

On the other hand, a Computational Fluid Dynamics (CFD) approach has been routinely employed in the field of naval architecture and ocean engineering owing to the merits that CFD can overcome the difficulties of nonlinear problems in theoretical studies while it is more cost-efficient compared to physical experiments [12–15]. Furthermore, the afore-mentioned shortcomings of Granville's method can be avoided using CFD. In CFD

simulations, the 3D effects can be considered and thus the ship resistance predictions can be more accurate. Furthermore, the CFD method is not only limited to ship hulls, but it can be applied for an arbitrary object in fluid. Accordingly, the CFD method has been used for investigating the roughness effect on ship resistance, e.g., [16–18], propeller performance, e.g., [19,20], and ship self-propulsion performance, e.g., [21,22], as well as the tidal turbine performance, e.g., [23].

Recently, Song et al. [24,25] validated Granville's method and the CFD method by comparing the predictions against a ship model test with a rough surface.

However, the majority of the studies have treated the hull surfaces as uniformly rough, while the real ships' surfaces are not uniform due to the heterogeneous biofouling accumulation on the hull. The simplification of treating the surfaces as uniformly rough can introduce inaccuracies in predicting the added resistance, as claimed by Demirel et al. [26].

Recently, Song et al. [27] conducted towing tests using a Wigley hull model with various hull roughness conditions including homogeneous conditions (i.e., smooth and full-rough) and heterogeneous conditions (i.e., $\frac{1}{4}$-bow-rough, $\frac{1}{4}$-aft-rough, $\frac{1}{2}$-bow-rough and $\frac{1}{2}$-aft-rough) by applying sand-grit on the hull surface systematically. Owing to the symmetric shape of the Wigley hull, the total resistance with the bow and aft-rough conditions could be compared to each other with the same rough surface areas. The result showed that the bow-rough conditions (i.e., $\frac{1}{4}$-bow-rough and $\frac{1}{2}$-bow-rough) showed larger added resistance than the aft-rough conditions (i.e., $\frac{1}{4}$-aft-rough and $\frac{1}{2}$-aft-rough). This finding suggests that the hull roughness in the forward part of the hull is more significant than other parts in terms of added resistance. This finding is attributed to the higher local skin friction near the leading edge, which is found either on smooth or rough surfaces. Song et al. [26] suggest that this higher local skin friction near the leading edge results in a higher roughness Reynolds number and thus a more significant roughness effect acts at the forward part of the hull. However, the study could not confirm the underlying cause since the local skin friction on the hull was not determined whilst measuring the total drag of the model.

On the other hand, there have been recent studies modelling the heterogeneous hull roughness in CFD simulations. Östman et al. [28] conducted CFD simulations of a full-scale tanker to investigate the potential in a low-cost approach for ship resistance reduction with selective applications of different quality coatings. In the CFD simulations, a high-quality coating (low roughness) surface was applied on the regions where high skin friction is concentrated, while the rest of the hull was modelled with a low-quality coating (high roughness). The result showed that the low-cost approach can reduce the ship resistance compared to the case when the low-quality coating is applied on the entire hull. Vargas et al. [29] investigated the impact of homogeneous and heterogeneous roughness distributions using CFD. A full-scale combatant was modelled with divided hull sections to evaluate different hull roughness scenarios. The result showed that the increase in the local skin friction due to hull roughness is highest at the bow, followed by sides, flat bottom, stern and transom, suggesting the benefits of partial hull cleaning. However, while these studies showed that the CFD simulations can be used to model the heterogenous hull roughness, their results were not validated against experimental data. Therefore, there is a need for a dedicated validation study to demonstrate the validity of the CFD approaches for predicting the effects of heterogeneous hull roughness.

The aim of the present study is, therefore, to fill this research gap by conducting CFD simulations to predict the effect of heterogeneous hull roughness on ship resistance and also performing a validation study by comparing the results with experimental data. In addition, the CFD simulations enable us to examine the local skin friction and roughness Reynolds number on the hull, and thus the locally varying flow regime over the heterogeneous hull roughness can be examined.

In this study, CFD simulations of the Wigley hull were developed with different hull roughness conditions using the modified wall-function approach with the roughness function model of the sand-grain surface, which were determined from previous

studies [24,25]. The CFD simulations of the Wigley hull model were performed with different hull conditions. The predicted total resistance coefficients for the various hull conditions were compared with the experimental data [27] for validation purposes. Finally, the local skin friction and the roughness Reynolds number distribution on the hull surfaces were correlated with the findings of the effect of heterogeneous roughness.

## 2. Methodology

### 2.1. Approach

Figure 1 schematically illustrates the methodology used in this study. An Unsteady Reynolds Averaged Navier–Stokes (URANS)-based CFD model was developed to replicate the physical Wigley hull model test of Song et al. [27]. The different hull roughness conditions were modelled using the modified wall-function approach with the roughness function model ($\Delta U^+$) of Song et al. [25]. The CFD simulations were performed with different hull conditions and compared with the towing test results [27]. Finally, the local wall shear stress and the roughness Reynolds number on the hull surfaces were examined to be correlated with the findings.
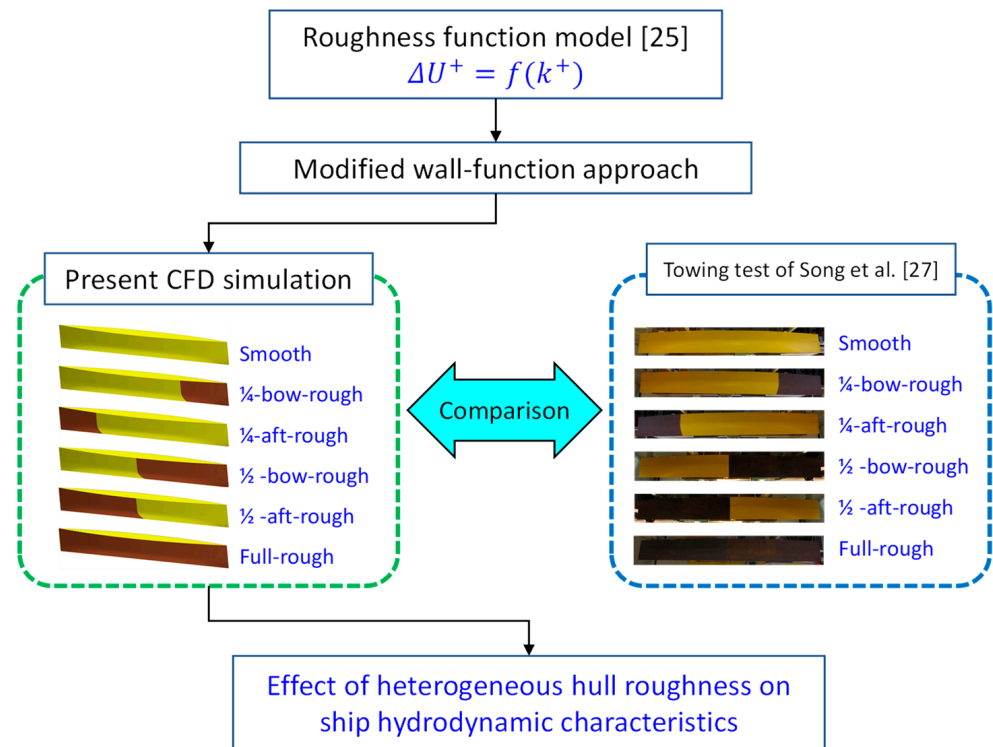


**Figure 1.** Schematic illustration of the current methodology.

### 2.2. Numerical Modelling

2.2.1. Mathematical Formulations

The URANS method was used to solve the governing equations using STAR-CCM+. The averaged continuity and momentum equations for incompressible flows can be given as

$$\frac{\partial(\rho \overline{u}_i)}{\partial x_i} = 0 \tag{1}$$

$$\frac{\partial(\rho \overline{u}_i)}{\partial t} + \frac{\partial}{\partial x_j}\left(\rho \overline{u}_i \overline{u}_j + \rho \overline{u_i' u_j'}\right) = -\frac{\partial \overline{p}}{\partial x_i} + \frac{\partial \overline{\tau}_{ij}}{\partial x_j} \tag{2}$$

where, $\rho$ is the fluid density, $\bar{u}_i$ is the time-averaged velocity vector, $\overline{\rho u_i' u_j'}$ is the Reynolds stress, $\bar{p}$ is the time-averaged pressure, $\bar{\tau}_{ij}$ is the mean viscous stress tensor components. This viscous stress for a Newtonian fluid can be expressed as

$$\bar{\tau}_{ij} = \mu \left( \frac{\partial \bar{u}_i}{\partial x_j} + \frac{\partial \bar{u}_j}{\partial x_i} \right) \tag{3}$$

In which, $\mu$ is the dynamic viscosity. The governing equations were discretised using the finite volume method with a second-order convection scheme and a first-order temporal discretisation. The $k$-$\omega$ SST turbulence model [30] was adopted to capture the turbulent flow, which combines the advantages of the $k$-$\omega$ and the $k$-$\varepsilon$ turbulence models. For the free surface effects, the Volume of Fluid (VOF) method was used.

### 2.2.2. Modified Wall-Function Approach

The roughness effect causes a downward shift of the velocity profile in the turbulent boundary layer. This downward shift is often called the "roughness function", $\Delta U^+$. With the roughness function, $\Delta U^+$, the log-law of the turbulent boundary layer can be written as

$$U^+ = \frac{1}{\kappa} \ln y^+ + B - \Delta U^+ \tag{4}$$

In which, $U^+$ is non-dimensional velocity defined as the ratio between the mean velocity, and the frictional velocity (i.e., $U^+ = U/U_\tau$). $U_\tau$ is defined as $\sqrt{\tau_w/\rho}$ where $\tau_w$ is the wall shear stress and $\rho$ is the fluid density. $y^+$ is the non-dimensional length defined as $yU_\tau/\nu$, in which $y$ is the normal distance from the wall and $\nu$ is the kinematic viscosity. $\kappa$ is the von Karman constant (=0.42) and $B$ is the log-low intercept.

The roughness function, $\Delta U^+$ is a function of roughness Reynolds number, $k^+$, defined as

$$k^+ = \frac{kU_\tau}{\nu} \tag{5}$$

In which, $k$ is the roughness height of the surface. The modified wall-function Equation (1) can be employed in CFD simulations to predict the roughness effect in the flow over the rough wall.

Song et al. [24] evaluated the roughness function of the sand grit (60/80 grit aluminium oxide abrasive powder) from the results of flat plate towing tests. Later on, a mathematical model of the roughness function (i.e., roughness function model) was proposed by Song et al. [25] to be used in CFD simulations.

As the same sand grit was used for the Wigley hull towing test [27], the same modified wall-function approach [25] was employed in this study to model the heterogeneous hull roughness conditions in CFD simulations. As proposed by Song et al. [25], the roughness function model for the 60/80 grit sand grain surface can be written as

$$\Delta U^+ = \begin{cases} 0 & \rightarrow & k^+ < 3 \\ \frac{1}{\kappa} \ln\left(0.49k^+ - 3\left(\frac{k^+ - 3}{25 - 3}\right)\right) \sin\left[\frac{\pi}{2} \frac{\log(k^+/3)}{\log(25/3)}\right] & \rightarrow & 3 \le k^+ < 25 \\ \frac{1}{\kappa} \ln(0.49k^+ - 3) & \rightarrow & 25 \le k^+ \end{cases} \tag{6}$$

where $k^+$ is the roughness Reynolds number based on the peak roughness height over a 50 mm interval (i.e., $k = Rt_{50} = 353$ μm). As shown in Figure 2, the roughness function model of Song et al. [25] agrees well with the experimental roughness function [24].
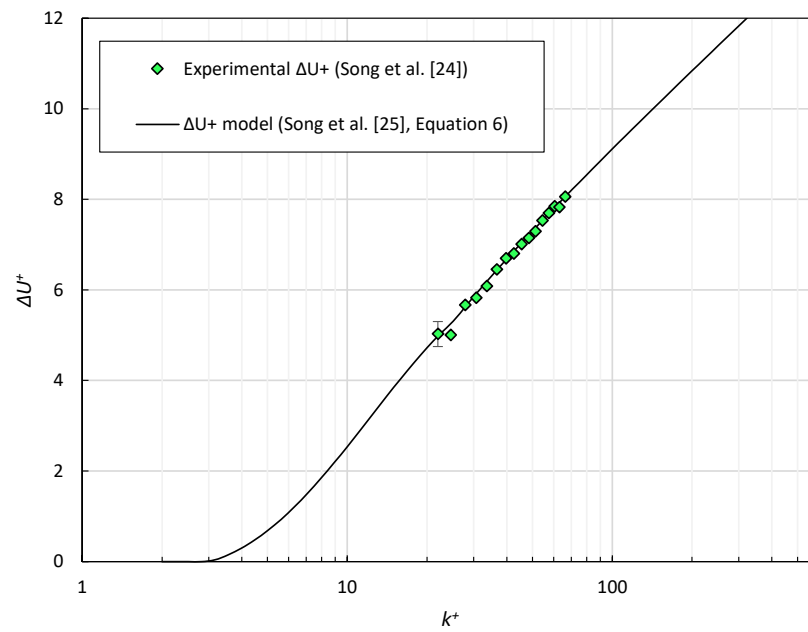
**Figure 2.** Experimental roughness function of Song et al. [24] and the roughness function model of Song et al. [25] Equation (6).

### 2.2.3. Geometry and Boundary Conditions

The Wigley hull is a parabolic hull form represented as

$$y = \frac{B}{2}\left[1 - \left(\frac{2x}{L}\right)^2\right]\left[1 + \left(\frac{z}{T}\right)^2\right] \tag{7}$$

where, $L$, $B$ and $T$ are the length, waterline beam and the draught of the model. In the current CFD simulations, the Wigley hull was modelled using the principal particulars used for the physical towing tests of Song et al. [27] as shown in Table 1.

**Table 1.** Principal particulars of the Wigley model and simulation conditions.

| Length | $L$ (m) | 3.00 |
|---|---|---|
| Beam at waterline | $B$ (m) | 0.30 |
| Draft | $T$ (m) | 0.1875 |
| Beam/draft ratio | $B/T$ | 1.6 |
| Total wetted surface area | $S$ (m$^2$) | 1.3383 |
| Wetted surface area of first quarter | $S_{Q1}$ (m$^2$) | 0.3066 |
| Wetted surface area of first half | $S_{H1}$ (m$^2$) | 0.6691 |
| Displacement | $\nabla$ (m$^3$) | 0.0750 |
| Block coefficient | $C_B$ | 0.4444 |
| Towing speed | V (m/s) | 1.08–2.17 |
| Froude number | $Fr$ | 0.2–0.4 |
| Reynolds number | $Re_L$ | 2.6–5.3 × 106 |
| Water temperature | $T_w$ (°C) | 12 |

As shown in Figure 3, the different hull roughness conditions tested by Song et al. [27] were modelled in CFD simulations. It is of note that the four regions of the Wigley hull have the same longitudinal length (i.e., $L/4$).

**Figure 3.** Different hull conditions of the Wigley hull simulations.

Figure 4 depicts the computational domain and the boundary conditions of the Wigley hull simulations used in this study. The computational domain size was chosen to be similar to that used by Dogrul et al. [31]. The velocity inlet boundary conditions were used for the inlet, top and bottom boundaries while the pressure outlet boundary condition was used for the outlet boundary. The centre midplane was defined as a symmetry plane. The no-slip wall boundary condition was used for the hull surface whilst simultaneously using different wall-functions. In other words, the modified wall-function, i.e., Equation (1) was used for the rough surfaces and the smooth-type wall-function (i.e., Equation (1) with $\Delta U^+ = 0$) is used for the smooth surfaces. The model was free to heave and sink in the simulations.
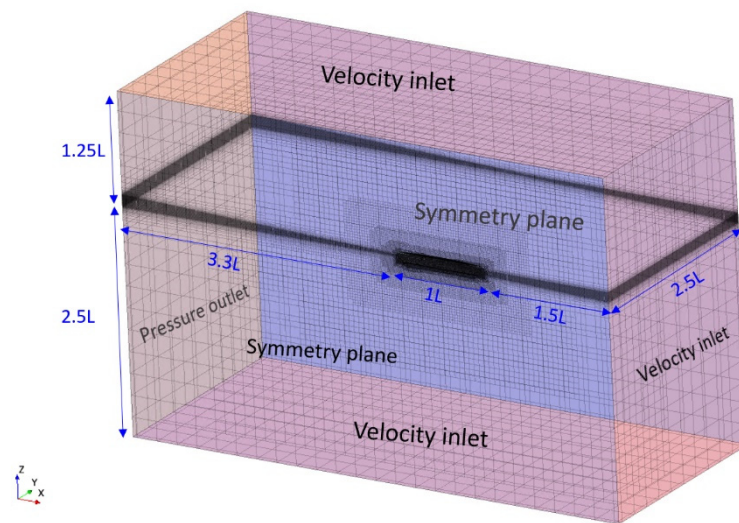


**Figure 4.** Computational domain and the boundary conditions of the Wigley hull simulation.

### 2.2.4. Mesh Generation

Figure 5 shows the grid structure used for the CFD simulations. The mesh generation was performed using the automated mesher of STAR-CCM+, with the Cartesian cut-cell method. The wall $y^+$ values were kept higher than 30 as well as the $k^+$ values as recommended by Siemens [32], as shown in Figure 6. It should be noted that the same mesh was used for all the simulations regardless of the surface conditions.
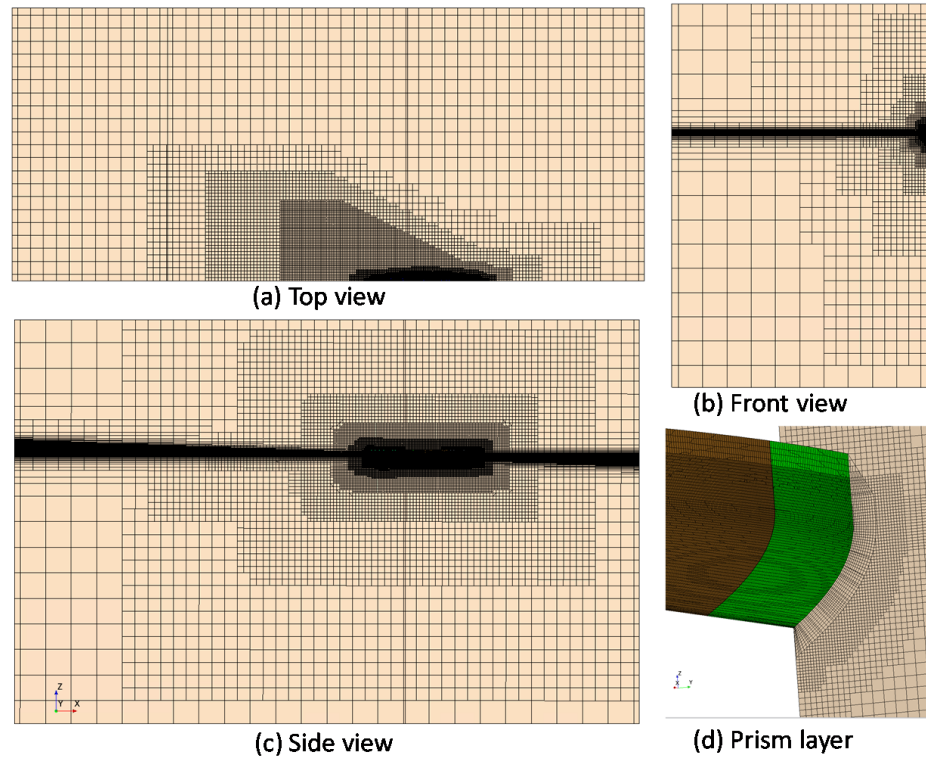


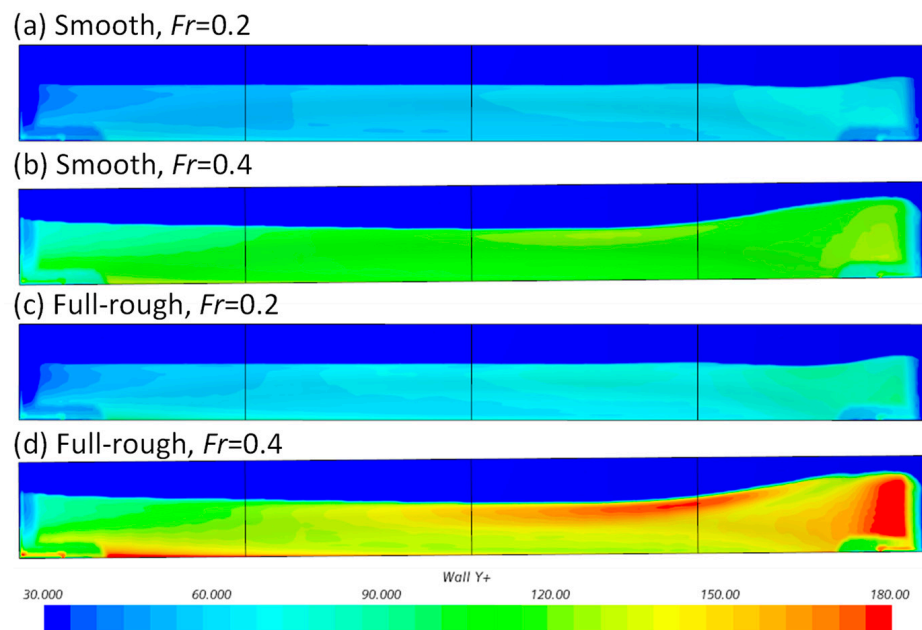**Figure 5.** Volume mesh of the Wigley hull simulation.



**Figure 6.** Wall y + on the Wigley hull.

## 3. Results

### 3.1. Verification Study

Spatial and temporal verification studies were performed to estimate the numerical uncertainties of the CFD model. The Wigley hull CFD simulations were conducted using three different resolutions of grids and time steps (i.e., Fine, Medium and Coarse), at $Fr = 0.3$ with the smooth hull condition. The Grid Convergence Index (GCI) method [33] was used to determine the spatial and temporal uncertainties ($U_{Grid}$ and $U_{\Delta t}$) in the total resistance coefficient, $C_T$, predictions as similarly used by other recent studies.

Table 2 shows the $U_{Grid}$ and $U_{\Delta t}$ values estimated from the convergence studies. As shown in the Table 2, $U_{Grid}$ and $U_{\Delta t}$ for the Wigley hull simulation are 0.053% and 0.022%, respectively, resulting in $U_{Total}$ of 0.057%. It is of note that the following simulation results were obtained using the fine mesh and fine time step.

**Table 2.** Spatial and temporal convergence study of the Wigley hull simulation, $Fr = 0.3$, smooth hull.

| Spatial Convergence | | No.Cells | $\Delta t$ (s) | $C_T$ |
|---|---|---|---|---|
| | Coarse | 414,173 | 0.01 | $5.292 \times 10^{-3}$ |
| | Medium | 776,227 | 0.01 | $5.273 \times 10^{-3}$ |
| | Fine | 1,587,310 | 0.01 | $5.267 \times 10^{-3}$ |
| $U_{Grid}$ (Fine) | | | | 0.053% |
| **Temporal Convergence** | | **No.Cells** | **$\Delta t$ (s)** | **$C_T$** |
| | Coarse | 1,587,310 | 0.04 | $5.169 \times 10^{-3}$ |
| | Medium | 1,587,310 | 0.02 | $5.258 \times 10^{-3}$ |
| | Fine | 1,587,310 | 0.01 | $5.267 \times 10^{-3}$ |
| $U_{\Delta t}$ (Fine) | | | | 0.022% |
| $U_{Total}$ | | | | 0.057% |

### 3.2. Effect of Heterogeneous Roughness on Ship Resistance

The Wigley hull CFD simulations were performed with various hull conditions at the speed range of $Fr = 0.2 - 0.4$, with the corresponding Reynolds numbers of $Re_L = 2.6 - 5.3 \times 10^6$. Figures 7–9 compare the total resistance coefficient, $C_T$, of the Wigley hull with the different hull roughness conditions obtained from the current CFD simulations and the Experimental Fluid Dynamics (EFD) results of Song et al. [27]. The $C_T$ values were calculated by as

$$C_T = \frac{R_T}{\frac{1}{2}\rho S V^2} \tag{8}$$

where $R_T$ is total resistance, $\rho$ is the density of water, $S$ is the wetted surface area, and $V$ is the towing speed (i.e., inlet velocity). As can be seen in Figure 7, the current CFD result agrees well with the experimental data of Song et al. [27]. This confirms the validity of the modified wall-function approach as previously demonstrated by Song et al. [25].

Figures 8 and 9 show the $C_T$ values of the Wigley hull with the heterogeneous hull roughness conditions (i.e., $\frac{1}{4}$-bow-rough, $\frac{1}{4}$-aft-rough, $\frac{1}{2}$-bow-rough and $\frac{1}{2}$-aft-rough). As observed from the physical towing tests of Song et al. [27], the current CFD simulations predicted larger $C_T$ values for the bow-rough conditions ($\frac{1}{4}$-bow-rough and $\frac{1}{2}$-bow-rough) than the aft-rough conditions ($\frac{1}{4}$-aft-rough and $\frac{1}{2}$-aft-rough). The percentage differences between the CFD and EFD results can be found from Table A1 in Appendix A.

Figures 10 and 11 compare the frictional and residuary resistance coefficients, $C_F$ and $C_R$, with the different hull conditions, respectively. The frictional and residuary resistance were calculated by simply decomposing the total drag into the shear and pressure components. The $C_F$ and $C_R$ were calculated as

$$C_F = \frac{R_F}{\frac{1}{2}\rho S V^2} \tag{9}$$

$$C_R = \frac{R_R}{\frac{1}{2}\rho S V^2} \tag{10}$$

where, $R_F$ and $R_R$ are the frictional (shear) and residuary (pressure) resistance, respectively.
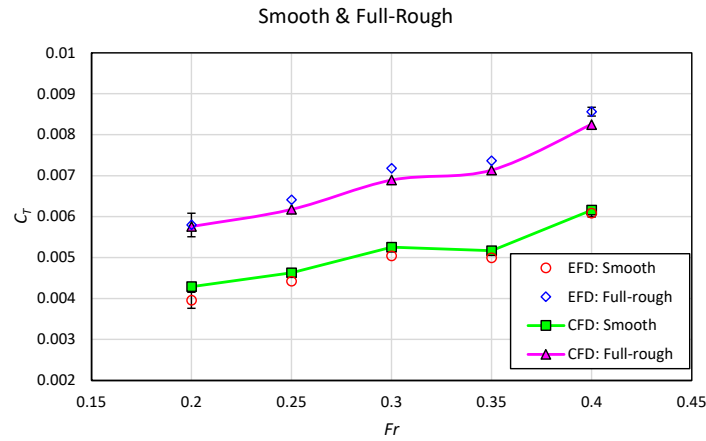


**Figure 7.** $C_T$ of the Wigley hull with smooth and full-rough conditions obtained from the current Computational Fluid Dynamics (CFD) simulations and the Experimental Fluid Dynamics (EFD) result [27].
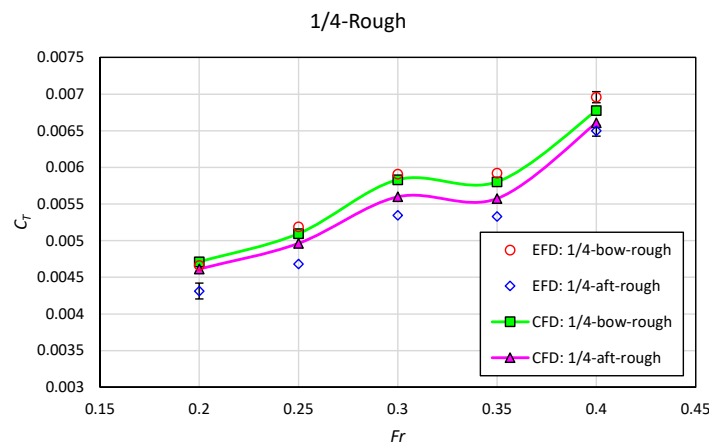


**Figure 8.** $C_T$ of the Wigley hull with $\frac{1}{4}$-bow-rough and $\frac{1}{4}$-aft-rough conditions obtained from the current CFD simulations and the EFD result [27].



**Figure 9.** $C_T$ of the Wigley hull with $\frac{1}{2}$-bow-rough and $\frac{1}{2}$-aft-rough conditions obtained from the current CFD simulations and the EFD result [27].

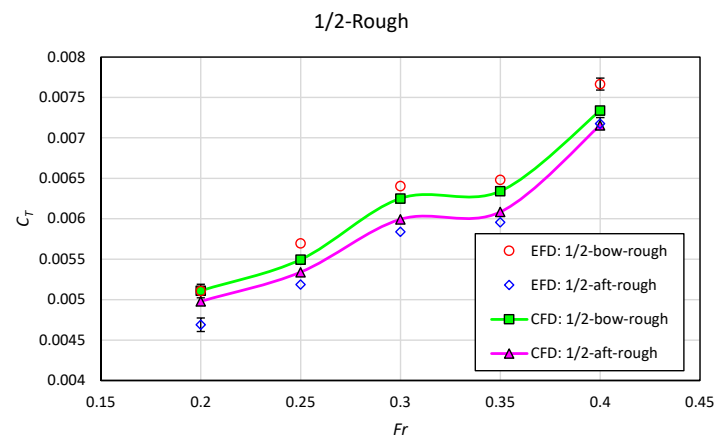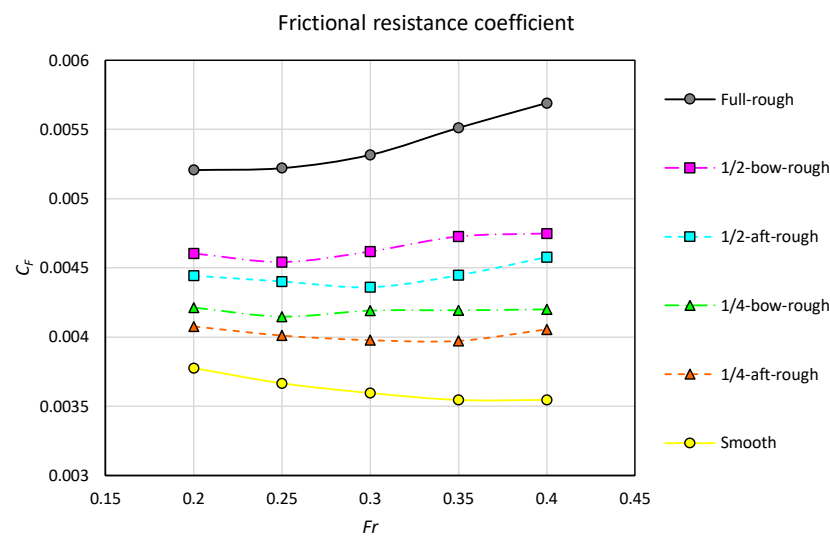Frictional resistance coefficient



**Figure 10.** $C_F$ of the Wigley hull with different hull conditions predicted from the current CFD simulations.
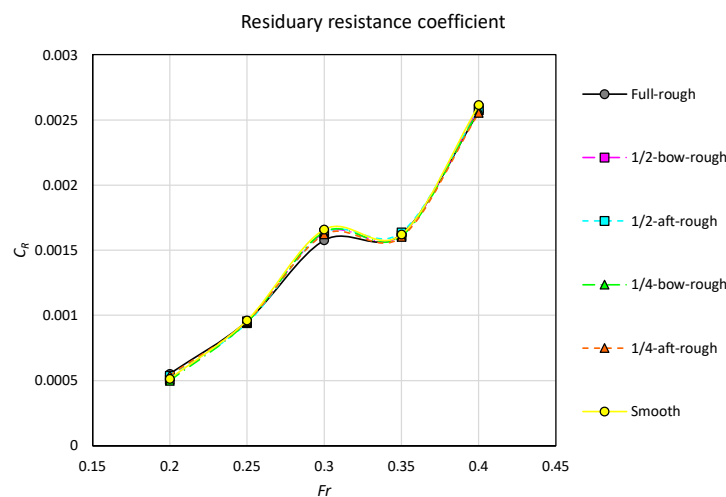
Residuary resistance coefficient



**Figure 11.** $C_R$ of the Wigley hull with different hull conditions predicted from the current CFD simulations.

As shown in Figures 10 and 11, the effect of different hull conditions on the $C_F$ values is apparent as expected, while the effect on the $C_R$ value is negligible. As expected, in Figure 10, the $C_F$ values of the smooth case show a descending trend while the $C_F$ values of the full-rough case show an ascending trend, which implies that the flow of each case is within the hydraulically smooth and transitionally rough flow regimes, respectively.

The bow-rough conditions show larger $C_F$ values than the aft-rough conditions with the same area of the rough surface. Accordingly, the differences in the added resistance between the bow-rough and aft-rough conditions can be mainly attributed to the different effects on the frictional resistance of the ship. Therefore, it is worthwhile to examine the effect of heterogeneous hull roughness on the distributions of the local skin friction on the hull.

Furthermore, in Figure 10, the $C_F$ trends of the different hull conditions show different transition behaviours in terms of roughness flow regimes. In other words, the bow-rough cases show more developed flow features at the same speed range than the aft-rough cases. For example, the $C_F$ values of the $\frac{1}{4}$-bow-rough case converge when $Fr > 0.3$ (i.e., the fully rough regime is reached), while those of the $\frac{1}{4}$-aft-rough case keep increasing (i.e., still within transitionally rough regime). For a similar reason, $C_F$ values of the full-rough case

keep increasing, although its forepart is expected to reach the fully rough regime because its aft part is still within the transitionally rough regime. The locally different flow regimes on the hull can be further correlated with the roughness Reynolds number, $k^+$, on the hull.

### 3.3. Rationale behind the Effect of Heterogeneous Roughness

As discussed in the previous section, the effect of heterogeneous hull roughness on ship resistance is believed to be closely related to the distributions of the local skin friction and the roughness Reynolds number. Therefore, this section discusses and compares the local skin friction, and the roughness Reynolds numbers with different hull conditions.

Figure 12 compares the local skin friction, $C_f$, values on the Wigley hull with different hull conditions. The local skin friction was obtained by dividing the wall shear stress, $\tau_w$, by the dynamic pressure, $\frac{1}{2}\rho V^2$, where $\rho$ is water density and $V$ is the towing speed (i.e., inlet velocity). As shown in Figure 12, significant increases in the local $C_f$ due to the roughness effect were observed. In the case of the homogeneous conditions (smooth and full-rough), the highest local $C_f$ values are observed in the first quarter of the hull. The heterogeneous hull conditions (Figure 12b–e) showed blended $C_f$ distributions, where the smooth surfaces show similar $C_f$ distributions as the smooth condition, while the rough surfaces show those similar to the full-rough condition. For example, the first quartile of the $\frac{1}{4}$-bow-rough case (Figure 12b) has a similar $C_f$ distribution as that of the full-rough case, while the rest of the hull has a similar $C_f$ distribution as that of the smooth case. As the full-rough condition has higher values in the bow region, the increase in the $C_f$ values of the bow-rough cases (Figure 12b,d) are more apparent compared to the aft-rough cases.
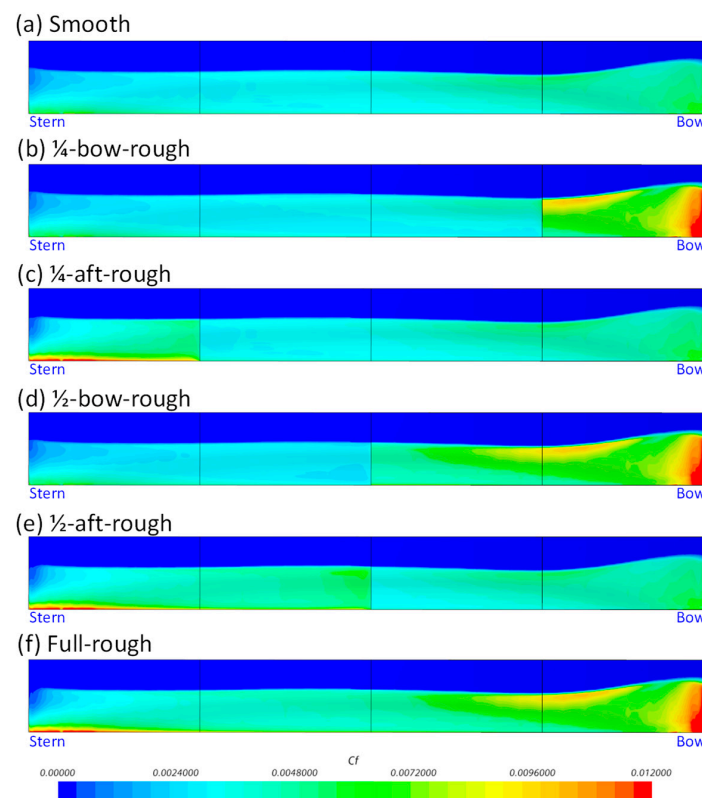


**Figure 12.** $C_f$ distribution on the Wigley hull with different hull conditions, $Fr = 0.3$.

Figure 13 clearly shows the increase in the $C_f$ values due to the presented hull roughness (i.e., $\Delta C_f = C_{f, \text{rough}} - C_{f, \text{smooth}}$). The full-rough case shows greater $\Delta C_f$ in the bow region, and thus the bow-rough conditions show larger $\Delta C_f$ values compared to the aft-rough conditions. The locally different $\Delta C_f$ values suggest different roughness effects in the different regions, and it can be best attributed to the different roughness Reynolds numbers, $k^+$, in the local regions.

(a) ¼-bow-rough
(b) ¼-aft-rough
(c) ½-bow-rough
(d) ½-aft-rough
(e) Full-rough

**Figure 13.** Increase in the $C_f$ on the Wigley hull ($\Delta C_f = C_{f,\text{rough}} - C_{f,\text{smooth}}$), $Fr = 0.3$.

Figure 14 shows the distributions of the roughness Reynolds number, $k^+$, on the Wigley hull with different hull roughness conditions. As expected, the full-rough case shows larger $k^+$ values in the bow region due to higher local skin friction (i.e., $k^+ = k\tau_w/\nu$). For a similar reason, the bow-rough cases show larger $k^+$ values compared to the aft-rough cases, and these differences result in different $\Delta C_f$ values. This observation supports the hypothesis of Song et al. [27].



(a) Smooth
(b) ¼-bow-rough
(c) ¼-aft-rough
(d) ½-bow-rough
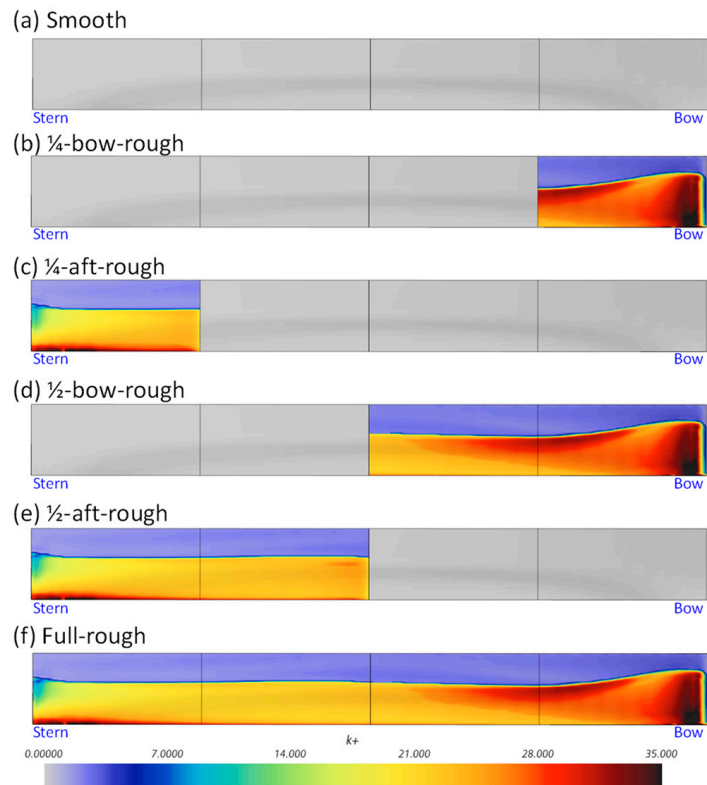(e) ½-aft-rough
(f) Full-rough

**Figure 14.** $k^+$ distribution on the Wigley hull with different hull conditions, $Fr = 0.3$.

The observations in Figures 12–14, with regards to $C_f$ and $k^+$, are in correspondence with the effect of different heterogeneous hull roughness on ship resistance shown in Figures 7–10. In other words, it can be seen that the greater increases in the $C_f$ and $k^+$ of the bow-rough cases resulted in the greater added resistances compared to the aft-rough cases as shown in Figures 7–10.

Furthermore, the $k^+$ values in Figure 14 can be also correlated with the different trends of the $C_F$ with different hull conditions in Figure 10. As shown in Equation (6), when $k^+$ value is higher than 25, it is considered that the fully rough flow regime is reached. Therefore, for example, it can be seen that the fully rough flow regime is reached for most of the rough wetted surface of the $\frac{1}{4}$-bow-rough condition (Figure 10), while the transitionally rough flow regime is expected for most of the wetted surface of the $\frac{1}{4}$-aft-rough condition (Figure 10).

Figure 15 shows the boundary layers represented by the axial velocity contours limited to $V_x/V_{ship} = 0.9$. When it comes to the homogeneous hull conditions, the results were as expected. The full-rough case (Figure 15b) shows a thicker boundary layer compared to the smooth case (Figure 15a) and the difference becomes more apparent along with the flow, as similarly observed from previous studies, e.g., [17,18,25]. On the other hand, differences were observed with the heterogeneous hull conditions. As shown in Figures 14f and 15d, the boundary layer thicknesses around the forward part of the aft-rough conditions (where the surface is smooth) showed almost no differences compared to that of the smooth case (Figure 15a). In contrast, the bow-rough conditions (Figure 15c,e) showed increases in the boundary layer thickness not only around the forward parts (where the surface is rough) but also around the aft parts (where the surface is smooth), compared to the smooth case (Figure 15a). Interestingly, the bow-rough conditions showed thicker boundary layers on the aft parts compared to the aft-rough conditions. For example, the $\frac{1}{2}$-bow-rough condition (Figure 15e) shows a thicker boundary layer than the $\frac{1}{2}$-aft-rough condition (Figure 15f) even around the aft part.
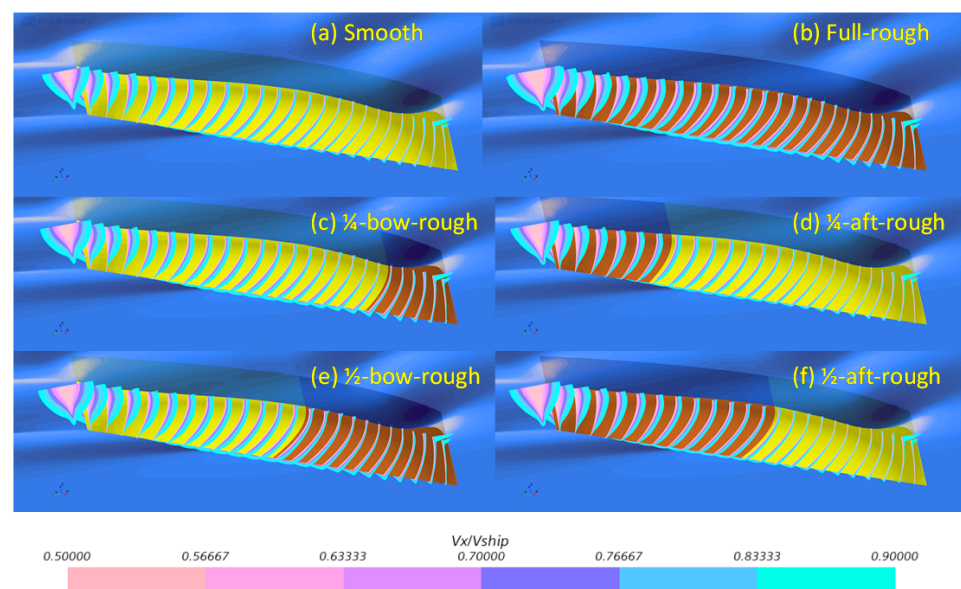


**Figure 15.** Boundary layer represented by slices limited to axial velocity ($V_x/V_{ship} = 0.9$), $Fr = 0.3$.

## 4. Concluding Remarks

A numerical investigation was completed on the effect of heterogeneous hull roughness on ship resistance. A URANS-based CFD model was developed to investigate the effect of heterogeneous hull roughness using the modified wall-function approach. The predicted total resistance coefficients with different hull conditions were compared with the experiment of Song et al. [27] and showed a good agreement. As similarly observed

by Song et al. [27], the bow-rough conditions showed larger added resistance compared to the aft-rough conditions with the same wetted surface area of the roughness region, confirming that the hull roughness of the fore part of the ship has a greater impact on the results than the hull roughness in other regions.

The observations on the effects of heterogeneous hull roughness were correlated with the distributions of the local wall shear stress and the roughness Reynolds number. The results showed that the local differences in the wall shear stress result in different roughness Reynolds numbers and thus different roughness effects depending on the locations of the hull roughness. Therefore, the hypothesis of Song et al. [27] was confirmed in this study.

This study provides a numerical investigation into the effect of heterogeneous hull roughness using the modified wall-function approach. The results can be useful from an industrial point of view, since they give insight into different priorities of partial hull cleaning depending on the impact of the roughness in different hull regions.

The investigation was carried out in model-scale using idealised surface conditions. However, the same methodology can be extended to incorporate real hull conditions of ships where heterogeneous biofouling accumulations are present. Furthermore, the numerical approach presented in this study can also be adopted for predicting the effect of heterogeneous roughness on propellers.

**Appendix A**

**Table A1.** Percentage differences between the current CFD simulations and the EFD result [27].

| | Smooth | | | 1/4-bow-rough | | | 1/4-aft-rough | | |
|---|---|---|---|---|---|---|---|---|---|
| *Fr* | CFD | EFD | %D | CFD | EFD | %D | CFD | EFD | %D |
| 0.2 | $4.29 \times 10^{-3}$ | $3.95 \times 10^{-3}$ | $-8.0\%$ | $4.71 \times 10^{-3}$ | $4.66 \times 10^{-3}$ | $-1.1\%$ | $4.61 \times 10^{-3}$ | $4.31 \times 10^{-3}$ | $-6.5\%$ |
| 0.25 | $4.63 \times 10^{-3}$ | $4.38 \times 10^{-3}$ | $-5.3\%$ | $5.09 \times 10^{-3}$ | $5.19 \times 10^{-3}$ | $1.8\%$ | $4.96 \times 10^{-3}$ | $4.68 \times 10^{-3}$ | $-5.7\%$ |
| 0.3 | $5.25 \times 10^{-3}$ | $5.03 \times 10^{-3}$ | $-4.3\%$ | $5.83 \times 10^{-3}$ | $5.91 \times 10^{-3}$ | $1.3\%$ | $5.60 \times 10^{-3}$ | $5.35 \times 10^{-3}$ | $-4.5\%$ |
| 0.35 | $5.17 \times 10^{-3}$ | $4.95 \times 10^{-3}$ | $-4.2\%$ | $5.80 \times 10^{-3}$ | $5.92 \times 10^{-3}$ | $2.0\%$ | $5.58 \times 10^{-3}$ | $5.33 \times 10^{-3}$ | $-4.4\%$ |
| 0.4 | $6.16 \times 10^{-3}$ | $6.08 \times 10^{-3}$ | $-1.4\%$ | $6.77 \times 10^{-3}$ | $6.96 \times 10^{-3}$ | $2.7\%$ | $6.61 \times 10^{-3}$ | $6.50 \times 10^{-3}$ | $-1.7\%$ |
| | 1/2-bow-rough | | | 1/2-aft-rough | | | Full-rough | | |
| *Fr* | CFD | EFD | %D | CFD | EFD | %D | CFD | EFD | %D |
| 0.2 | $5.11 \times 10^{-3}$ | $5.11 \times 10^{-3}$ | $-0.1\%$ | $4.98 \times 10^{-3}$ | $4.69 \times 10^{-3}$ | $-5.8\%$ | $5.76 \times 10^{-3}$ | $5.81 \times 10^{-3}$ | $0.9\%$ |
| 0.25 | $5.50 \times 10^{-3}$ | $5.70 \times 10^{-3}$ | $3.6\%$ | $5.34 \times 10^{-3}$ | $5.19 \times 10^{-3}$ | $-2.8\%$ | $6.18 \times 10^{-3}$ | $6.40 \times 10^{-3}$ | $3.6\%$ |
| 0.3 | $6.25 \times 10^{-3}$ | $6.40 \times 10^{-3}$ | $2.4\%$ | $5.99 \times 10^{-3}$ | $5.84 \times 10^{-3}$ | $-2.6\%$ | $6.89 \times 10^{-3}$ | $7.20 \times 10^{-3}$ | $4.5\%$ |
| 0.35 | $6.34 \times 10^{-3}$ | $6.48 \times 10^{-3}$ | $2.2\%$ | $6.08 \times 10^{-3}$ | $5.96 \times 10^{-3}$ | $-2.1\%$ | $7.13 \times 10^{-3}$ | $7.38 \times 10^{-3}$ | $3.4\%$ |
| 0.4 | $7.34 \times 10^{-3}$ | $7.66 \times 10^{-3}$ | $4.4\%$ | $7.15 \times 10^{-3}$ | $7.18 \times 10^{-3}$ | $0.3\%$ | $8.25 \times 10^{-3}$ | $8.58 \times 10^{-3}$ | $4.0\%$ |

## References

1. Townsin, R.L. The ship hull fouling penalty. *Biofouling* **2003**, *19*, 9–15. [CrossRef]
2. Tezdogan, T.; Demirel, Y.K. An overview of marine corrosion protection with a focus on cathodic protection and coatings. *Brodogradnja* **2014**, *65*, 49–59.
3. Granville, P.S. The frictional resistance and turbulent boundary layer of rough surfaces. *J. Ship Res.* **1958**, *2*, 52–74. [CrossRef]
4. Granville, P.S. *Similarity-Law Characterization Methods for Arbitrary Hydrodynamic Roughnesses*; Bethesda: Rockville, MD, USA, 1978.
5. Schultz, M.P. The relationship between frictional resistance and roughness for surfaces smoothed by sanding. *J. Fluids Eng.* **2002**, *124*, 492–499. [CrossRef]
6. Schultz, M.P. Frictional resistance of antifouling coating systems. *J. Fluids Eng.* **2004**, *126*, 1039–1047. [CrossRef]
7. Schultz, M.P.; Flack, K.A. The rough-wall turbulent boundary layer from the hydraulically smooth to the fully rough regime. *J. Fluid Mech.* **2007**, *580*, 381–405. [CrossRef]
8. Flack, K.A.; Schultz, M.P. Review of hydraulic roughness scales in the fully rough regime. *J. Fluids Eng.* **2010**, *132*, 041203. [CrossRef]
9. Schultz, M.P.; Bendick, J.A.; Holm, E.R.; Hertel, W.H. Economic impact of biofouling on a naval surface ship. *Biofouling* **2011**, *27*, 87–98. [CrossRef]
10. Oliveira, D.; Larsson, A.I.; Granhag, L. Effect of ship hull form on the resistance penalty from biofouling. *Biofouling* **2018**, *34*, 262–272. [CrossRef]
11. Atlar, M.; Yeginbayeva, I.A.; Turkmen, S.; Demirel, Y.K.; Carchen, A.; Marino, A.; Williams, D. A rational approach to predicting the effect of fouling control systems on "in-service" ship performance. *GMO J. Ship Mar. Technol.* **2018**, *24*, 5–36.
12. Cella, U.; Cucinotta, F.; Sfravara, F. Sail plan parametric CAD model for an A-class catamaran numerical optimization procedure using open source tools. In Proceedings of the 16th Asian Congress of Fluid Mechanics, Bangalore, India, 13–17 December 2019; pp. 547–554.
13. Cirello, A.; Cucinotta, F.; Ingrassia, T.; Nigrelli, V.; Sfravara, F. Fluid–structure interaction of downwind sails: A new computational method. *J. Mar. Sci. Technol.* **2019**, *24*, 86–97. [CrossRef]
14. Stern, F.; Wang, Z.; Yang, J.; Sadat-Hosseini, H.; Mousaviraad, M.; Bhushan, S.; Diez, M.; Sung-Hwan, Y.; Wu, P.-C.; Yeon, S.M.; et al. Recent progress in CFD for naval architecture and ocean engineering. *J. Hydrodyn.* **2015**, *27*, 1–23. [CrossRef]
15. Wang, J.; Wan, D. Application progress of computational fluid dynamic techniques for complex viscous flows in ship and ocean engineering. *J. Mar. Sci. Appl.* **2020**, *19*, 1–16. [CrossRef]
16. Demirel, Y.K.; Turan, O.; Incecik, A. Predicting the effect of biofouling on ship resistance using CFD. *Appl. Ocean Res.* **2017**, *62*, 100–118. [CrossRef]
17. Song, S.; Demirel, Y.K.; Atlar, M. An investigation into the effect of biofouling on the ship hydrodynamic characteristics using CFD. *Ocean Eng.* **2019**, *175*, 122–137. [CrossRef]
18. Song, S.; Demirel, Y.K.; Muscat-Fenech, C.D.M.; Tezdogan, T.; Atlar, M. Fouling effect on the resistance of different ship types. *Ocean Eng.* **2020**, *216*, 107736. [CrossRef]
19. Song, S.; Demirel, Y.K.; Atlar, M. Propeller performance penalty of biofouling: Computational fluid dynamics prediction. *J. Offshore Mech. Arct. Eng.* **2020**, *142*, 1–22. [CrossRef]
20. Farkas, A.; Degiuli, N.; Martić, I. The impact of biofouling on the propeller performance. *Ocean Eng.* **2021**, *219*, 108376. [CrossRef]
21. Song, S.; Demirel, Y.K.; Atlar, M. Penalty of hull and propeller fouling on ship self-propulsion performance. *Appl. Ocean Res.* **2020**, *94*, 102006. [CrossRef]
22. Farkas, A.; Song, S.; Degiuli, N.; Martić, I.; Demirel, Y.K. Impact of biofilm on the ship propulsion characteristics and the speed reduction. *Ocean Eng.* **2020**, *199*, 107033. [CrossRef]
23. Song, S.; Demirel, Y.K.; Atlar, M.; Shi, W. Prediction of the fouling penalty on the tidal turbine performance and development of its mitigation measures. *Appl. Energy* **2020**, *276*, 115498. [CrossRef]
24. Song, S.; Dai, S.; Demirel, Y.K.; Atlar, M.; Day, S.; Turan, O. Experimental and theoretical study of the effect of hull roughness on ship resistance. *J. Ship Res.* **2020**, 1–10. [CrossRef]
25. Song, S.; Demirel, Y.K.; Atlar, M.; Dai, S.; Day, S.; Turan, O. Validation of the CFD approach for modelling roughness effect on ship resistance. *Ocean Eng.* **2020**, *200*, 107029. [CrossRef]
26. Demirel, Y.K.; Uzun, D.; Zhang, Y.; Fang, H.-C.; Day, A.H.; Turan, O. Effect of barnacle fouling on ship resistance and powering. *Biofouling* **2017**, *33*, 819–834. [CrossRef]
27. Song, S.; Ravenna, R.; Dai, S.; De Marco Muscat-Fenech, C.; Tani, G.; Demirel, Y.K.; Atlar, M.; Day, S.; Incecik, A. Ex-perimental investigation on the effect of heterogeneous hull roughness on ship resistance. *Ocean Eng.* **2021**, in press. [CrossRef]
28. Östman, A.; Koushan, K.; Savio, L. Study on additional ship resistance due to roughness using CFD. In Proceedings of the 4th Hull Performance & Insight Conference (HullPIC'19), Gubbio, Italy, 6–8 May 2019.
29. Vargas, A.; Shan, H.; Holm, E. Using CFD to predict ship resistance due to biofouling, and plan hull maintenance. In Proceedings of the 4th Hull Performance & Insight Conference (HullPIC'19), Gubbio, Italy, 6–8 May 2019.
30. Menter, F.R. Two-equation eddy-viscosity turbulence models for engineering applications. *AIAA J.* **1994**, *32*, 1598–1605. [CrossRef]
31. Dogrul, A.; Song, S.; Demirel, Y.K. Scale effect on ship resistance components and form factor. *Ocean Eng.* **2020**, *209*, 107428. [CrossRef]
32. Siemens. *STAR-CCM+, User Guide*, Version 13.06.
33. Celik, I.B.; Ghia, U.; Roache, P.J.; Freitas, C.J.; Coleman, H.; Raad, P.E. Procedure for estimation and reporting of uncertainty due to discretization in CFD applications. *J. Fluids Eng.* **2008**, *130*, 078001. [CrossRef]